ACS APPLIED MATERIALS & INTERFACES

Research Article

www.acsami.org

Highly Efficient Antibacterial Iron Oxide@Carbon Nanochains from Wüstite Precursor Nanoparticles

Shu F. Situ and Anna Cristina S. Samia*

Department of Chemistry, Case Western Reserve University, 10900 Euclid Avenue, Cleveland, Ohio 44106, United States

Supporting Information

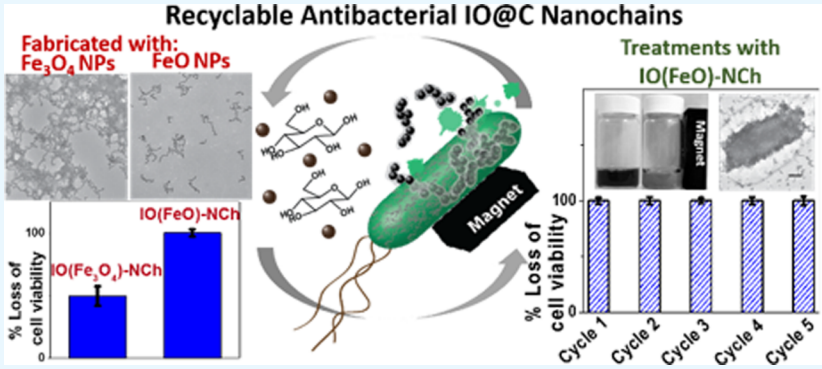

ABSTRACT: A new hydrothermal synthesis approach involving the carbonization of glucose in the presence of wüstite (FeO) nanoparticles is presented, which leads to the fabrication of rapidly acting and potent antibacterial agents based on iron oxide@carbon (IO@C) nanochains. By using nonmagnetic FeO precursor nanoparticles that slowly oxidize into the magnetic Fe_3O_4 crystal structure under hydrothermal conditions, we were able to prepare well-defined and short-length IO@C nanochains that are highly dispersed in aqueous media and readily interact with bacterial cells, leading to a complete loss in bacterial cell viability within short incubation times at minimal dosage. The smaller IO@C nanochains synthesized using the FeO precursor nanoparticles can reach above 2-fold enhancement in microbe-killing activity when compared to the larger nanochains fabricated directly from Fe_3O_4 nanoparticles. In addition, the synthesized IO@C nanochains can be easily isolated using an external magnet and be subsequently recycled to effectively eradicate *Escherichia coli* cells even after five separate treatment cycles.

KEYWORDS: *carbon-based nanomaterials, magnetic hybrid nanostructures, iron oxide nanoparticles, recyclable antibacterial agents, hydrothermal carbonization*

INTRODUCTION

Carbon-based nanomaterials are being heavily explored for their potential in antibacterial applications due to their capability to promote bacterial cell death through direct physical interactions and by means of chemical stress induced by the in situ production of reactive oxygen species (ROS).[1−14] In addition, since the bacterial cell wall contains receptor proteins that recognize carbohydrate moieties to promote faster intake of nutrients, carbon-based nanomaterials that mimic the carbohydrate molecular structure can have strong affinity for these microbes.[15] Furthermore, previous studies have suggested that by tuning the size, morphology, and surface chemistry of carbon-based nanomaterials, their bacteria inactivation properties can be drastically improved.[10−14,16,17] Several studies have demonstrated that well-dispersed single-walled carbon nanotubes showed increased toxicity compared to their aggregated multiwalled counterparts due to their enhanced bacterial cell interactions that promote their ability to rupture the cell membrane of these microbes.[11−14] Recently, Liu et al. have also demonstrated that dispersed graphene oxide nanosheets with sharp edges can readily destroy the membrane integrity of bacterial cells through the piercing of their outer cell membrane, while a reduced form of the graphene oxide nanosheets can easily aggregate and fall out of solution, thus, minimizing physical interactions with the bacterial cells.[12] Moreover, due to the high affinity of graphene oxide nanosheets for bacterial cells, these nanomaterials have been hybridized with other metal-based nanostructures, such as ZnO and Ag nanoparticles that can leach out toxic ions, in order to improve the localization of harmful metal ions at the bacterial cell surface.[2−4]

While carbon-based nanomaterials have demonstrated great potential in the treatment of bacterial contamination, the incorporation of a magnetic component that will facilitate easy isolation of the antibacterial agent after application is of high interest.[5,18] By integrating Fe_3O_4 nanoparticles into a graphene oxide/Ag hybrid nanomaterial system, Tian et al. were able to isolate the graphene oxide-based nanomaterial after antibacte-

Received: August 25, 2014
Accepted: October 14, 2014
Published: October 27, 2014

rial treatment, allowing the recycling of the multifunctional antibacterial agent.[5]

Although the successful incorporation of Fe_3O_4 nanoparticles into chain-like carbon nanostructures has been previously shown, the resulting large network of the hybridized magnetic nanomaterial often led to aggregation, which can compromise the antibacterial efficacy.[6,19] Here, we report for the first time the use of nonmagnetic FeO nanoparticles as precursors to prepare short-length and well-dispersed iron oxide@carbon (IO@C) nanochains that act as a cost-effective, reusable, and fast-acting antibacterial agent.

Over the past years, different synthesis methods have been developed to prepare carbon-based nanomaterials, including the use of arc-discharge,[20] chemical vapor deposition,[21] pyrolysis of organic compounds,[22] and hydrothermal carbonization (HTC).[23−27] In particular, the HTC process has been widely used to synthesize carbon-based nanomaterials because of its simplicity and use of natural carbohydrates that are readily available.[23−27] In the HTC process, carbon nanostructures are generated from the dehydration of simple sugars producing 5-(hydroxymethyl)furfural (HMF) that subsequently polymerize into polyfurans, which, in turn, undergo intermolecular condensation toward carbonization.[23−27] Depending on the carbon source, the HTC method can require up to 48 h of reaction time.[23−26] However, Cui et al. have demonstrated the accelerated carbonization of starch to form carbon nanospheres or nanoropes in the presence of metal catalysts.[27] Similarly, Zhang et al. prepared large carbon nanochain networks using 80 nm Fe_3O_4 nanoparticles as coreagents.[19] The formation of interconnected large nanochain networks may lead to dispersion instability and can be attributed to the strong magnetic dipolar interactions observed in ferrimagnetic Fe_3O_4 nanoparticles with diameters larger than 30 nm.[19,28−33] In this study, we report on an alternative one-step HTC synthesis approach to prepare functional magnetic hybrid nanostructures with carbon nanochains containing superparamagnetic Fe_3O_4 cores that were slowly oxidized from FeO precursor nanoparticles. The slow hydrothermal-assisted oxidization process of FeO into Fe_3O_4 can increase the magnetic dipolar interactions among the iron oxide nanoparticles at a controlled rate, aiding in the formation of short, well-defined nanoassemblies with chain-like morphology. Finally, we systematically evaluated the influence of the nanochain size, morphology, and carbon encapsulation on the inactivation of *Escherichia coli* (*E. coli*) culture cells.

EXPERIMENTAL SECTION

Materials and Reagents. The iron(III) chloride hexahydrate (98%), anhydrous iron(II) chloride (98%), oleic acid (90%), 1-octadecene (90%), glucose (99.5%), triethylamine (99%), toluene (HPLC grade, 99%), hexane (HPLC grade, 95%), ethanol (HPLC grade, 90%), and XTT (2,3-bis(2-methoxy-4-nitro-5-sulfophenyl)-2H-tetrazolium-5-carboxanilide) assay kit were purchased from Sigma-Aldrich. Sodium oleate (97%) was purchased from TCI America. Ammonium hydroxide (14.8 N), hydrochloric acid (37%), 3-(triethoxysilyl)propyl succinic anhydride (95%), hydrogen peroxide (30%), absolute ethanol, and the iron reference standard solution (1000 ppm) for the atomic absorption spectroscopic analyses were purchased from Fischer Scientific. The ultrapure Luria−Bertani (LB) agar powder used to prepare the bacterial culture plates was obtained from Affymetrix. The *E. coli* bacterial cell culture line was obtained from Invitrogen. All of the chemicals and reagents were used as received.

Synthesis of Iron Oxide Nanoparticles. The IO nanoparticles were synthesized according to a previously reported method.[34,35] The as-prepared FeO nanoparticles are coated in oleic acid and are well-dispersed in organic solvents such as toluene and hexane. In order to transfer the FeO nanoparticles into an aqueous phase, the surface of the FeO nanoparticles was modified through a ligand exchange process.[36] FeO nanoparticles dispersed in toluene (100 mg in 4 mL of toluene) were mixed with 4 mL of 1 M NH_4OH in 1-butanol, 1.4 mL of triethylamine, and 0.1 mL of 3-(triethoxysilyl)propyl succinic anhydride before adding 0.5 mL of deionized water. The mixture was vortex mixed for 3 min and left to stand at room temperature for 1 h. After 1 h, the ligand-exchanged FeO nanoparticles transferred from the top toluene layer into the bottom aqueous layer. To isolate the nanoparticles, the mixture was centrifuged for 30 min at 8000 rpm and the nanoparticles were redispersed in water prior to use as a coreagent in the hydrothermal carbonization of glucose.

Carbon Nanochain Synthesis. In a typical synthesis, 1 mmol of glucose (0.2 g) was dissolved in 10 mL of deionized water. After adding 65 mmol of FeO nanoparticles (4.7 mg) to the glucose solution, the mixture was transferred into a Teflon-lined stainless steel autoclave and heated to 180 °C for 2 to 24 h to prepare the 2h-NCh, 4h-NCh, 8h-NCh, 12h-NCh, and 24h-NCh samples, respectively. The product was cooled to room temperature and centrifuged at 8000 rpm for 60 min to ensure separation of the nanochains from the supernatant solution. The final product was washed and recentrifuged six more times to remove excess iron ions that leached out from the synthesized nanochains. To obtain nanochains without IO cores, the IO cores were dissolved from the IO@C nanochains by an overnight acid digestion treatment at 90 °C with concentrated HCl (37%) inside a Teflon-lined stainless steel autoclave.

Materials Characterization. A JEOL 1200CX transmission electron microscope (TEM) operated at 80 kV was used to evaluate the size and morphology of the IO nanoparticles and the IO@C nanochains. The software ImageJ was used to measure the particle size of an average of 200 particles to estimate the size distribution for each sample. The iron content in the different IO@C nanochain samples was evaluated using atomic absorption spectroscopy (AAS). Attenuated total reflectance−Fourier transform infrared spectroscopic (ATR-FTIR) analyses were conducted in the range 600−4000 cm^{-1} using a Thermo Scientific Nexus 870 ATR-FTIR spectrometer. The particle size of the nanochain dispersions was measured by dynamic light scattering (DLS) on a ZetaPALS particle size analyzer (Brookhaven) at a scattering angle of 90°. The field-dependent magnetic properties of the IO nanoparticles and the nanochains were evaluated at 5 K using a Quantum Design MPMS5 SQUID (Superconducting Quantum Interference Device) magnetometer.

The powder X-ray diffraction (PXRD) patterns of the samples were collected using a Rigaku MiniFlex X-ray powder diffractometer using Cu Kα radiation (γ = 0.154 nm). For Rietveld analysis, a 2-θ range from 20 to 70° was scanned at 0.01° step size at 1 s/step and used in the weight percentage calculation for the wüstite (FeO) and magnetite (Fe_3O_4) phases. To estimate the relative proportions of magnetite (Fe_3O_4) and maghemite (γ-Fe_2O_3) in the samples, the weight percentage of the iron oxide phases was estimated using a smaller 2-θ range from 55 to 60° that was scanned at 0.01° step size at 10 s/step. All of the peak profiles were fitted with pseudo-Voigt function and corrected with March−Dollase function.[37] The reference diffraction pattern standards were obtained from the International Centre for Diffraction Data (ICDD): FeO (#01-073-2143), Fe_3O_4 (#01-071-4918), γ-Fe_2O_3 (#01-089-5892).

Cell Viability Assays by Colony Counting Method. For all of the cell studies, the *E. coli* cell culture was diluted with deionized water to an $OD_{600\ nm}$ of 0.01 before use. In order to evaluate the effect of the IO nanoparticles on the *E. coli* growth, 100 μg of IO(FeO) nanoparticles dispersed in 10 μL deionized water was added to 990 μL of diluted cell culture (8×10^6 cells) and incubated at room temperature for 15 min before spreading 5 μL of the resulting mixture onto a LB agar plate. The agar plate containing the *E. coli* spread was cultured in an incubator at 37 °C overnight. The bacterial growth was evaluated through counting of the resulting colonies. The same

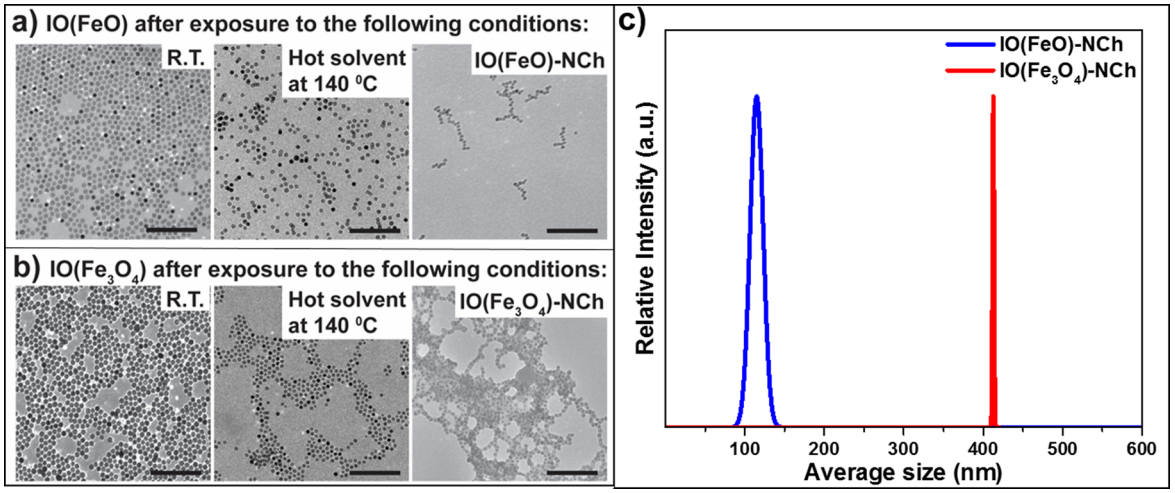

Figure 1. Corresponding transmission electron microscope (TEM) images of the (a) FeO and (b) Fe_3O_4 nanoparticle samples that were deposited onto the TEM grids after exposure to room temperature (RT) conditions, after heating the samples in solution to 140 °C under Ar gas, and after HTC treatment that results in nanochain formation after 4 h at 180 °C; the scale bars represent 200 nm for the TEM images. (c) Dynamic light scattering (DLS) measurements showing the comparison of the average size of the nanochains synthesized using FeO and Fe_3O_4 precursor nanoparticles, respectively.

procedure was performed with the following nanochain samples: 2h-NCh, 4h-NCh, 8h-NCh, 12h-NCh, and 24h-NCh. The antibacterial assay approach was also adapted in comparing the activities of the 4h-NCh sample with and without IO cores, as well as in the comparison of the antibacterial efficacy of the IO(FeO)-NCh and IO(Fe_3O_4)-NCh samples. For all the bacterial cell assays, 10 μL of deionized water was adapted as a control treatment to replace the IO/nanochain samples. All the nanochain samples were washed extensively with deionized water a total of six times prior to bacterial cell incubation to ensure removal of iron ions entrapped in the porous carbon shells. Statistical analyses were performed on the evaluated loss of cell viability data to test for differences among the different treatment groups. A one-way analysis of variance (ANOVA) was conducted with $n = 5$. Moreover, Student's t test was used to statistically compare paired sample sets. For the concentration-dependence assay, the concentration of the antibacterial agents was adjusted to 0, 50, 100, 200, 500, 750, and 1000 μg/mL, respectively.

Detection of Reactive Oxygen Species. The possible generation of ROS, such as the superoxide anion radical ($O_2^{\bullet-}$), was evaluated by monitoring the absorption of XTT (2,3-bis(2-methoxy-4-nitro-5-sulfophenyl)-2H-tetrazolium-5-carboxanilide). In the presence of ROS, the pale yellow XTT dye is reduced to its bright orange-colored XTT-formazan analog, the accumulation of which can be measured by monitoring its absorbance at 470 nm.[12,38−40] In our study, 100 μg of the IO nanoparticle/nanochain samples [i.e., IO(FeO), 2h-NCh, 4h-NCh with and without IO core, 8h-NCh, 12h-NCh, and 24h-NCh] were separately dispersed in 1 mL of deionized water prior to incubation with 20 μL of an *E. coli* cell suspension (8×10^6 cells). Afterward, 255 μL of XTT (1.5 mM with 1% phenazine methosulfate for prevention of inefficient reduction) was added to the different IO nanoparticle/nanochain cell suspensions and the mixtures were incubated in the dark at room temperature for 15 min or 5 h, respectively. Following incubation, the mixtures were centrifuged at 13 000 rpm for 1 min and the supernatants were filtered through 0.2 μm Acrodisk poly(ether sulfone) filters to remove the aggregated IO nanoparticles/nanochains and *E. coli* cells. The filtered solutions (200 μL) were then pipetted into a 96-well plate with four replicates for each sample treatment. The absorbances at 470 nm were measured on a FLUOstar Omega multimode microplate reader. In this assay, hydrogen peroxide (0.5, 1.0, 2.0 mM) was used as positive control. In addition, the XTT reduction in the absence of the *E. coli* cells was evaluated by replacing the cell suspension with deionized water.

Antibacterial Recyclability Studies. The 4h-NCh sample was magnetically separated from solution using a 1 T FeNdB bar magnet (2 in. × 1 in. × $^1/_2$ in.). *E. coli* cultures containing approximately 4×10^8 cells in 10 mL water were exposed to the isolated nanochain sample (5 mg) at room temperature for 15 min. After bacteria exposure, the nanochains were isolated using an external 1 T FeNdB bar magnet, and 5 μL of the treated bacterial cells were plated onto LB agar plates to estimate cell viability via the colony counting approach. To remove bacterial fragments attached to the nanochains, the magnetically isolated nanochains were mixed with absolute ethanol and sonicated for 30 min before isolation with a bar magnet. This washing step was repeated a total of five times. The same procedure was repeated three times using deionized water, and the nanochains were vacuum-dried to remove ethanol/water residue before the next antibacterial treatment cycle.

RESULTS AND DISCUSSION

Formation of IO@C Nanochains. To fabricate the hybrid magnetic carbon nanochains, IO nanoparticles were used as coreagents during the HTC of glucose. The unique magnetic dipolar interactions between the IO nanoparticles dictate their self-assembly behavior at elevated temperatures, which in turn influence the morphology of the resulting IO@C nanochains during HTC.[28−33] Basically, IO nanoparticles can adapt several common crystalline phases, each with highly distinct magnetic properties.[41] When exposed to high temperatures (>120 °C) under aerobic conditions, wüstite (FeO), which is the most reduced IO form, will first oxidize to magnetite (Fe_3O_4), and further oxidation of the divalent iron ion will give rise to the maghemite (γ-Fe_2O_3) crystalline phase. Among the previously discussed IO phases, Fe_3O_4 exhibits the highest saturation magnetization, while FeO is largely nonmagnetic in nature (Supporting Information Figure S1).[41]

At room temperature (RT), both FeO and Fe_3O_4 nanoparticles, with an average diameter of 15 nm, were freely dispersed in solution and no chain-like assemblies were observable under TEM in the absence of an external magnetic field or sufficient thermal activation energy, which can enable them to cohesively realign their magnetic moments (Figure 1a, b). However, at elevated temperatures, the IO nanoparticles can be thermally activated and in particular the super-

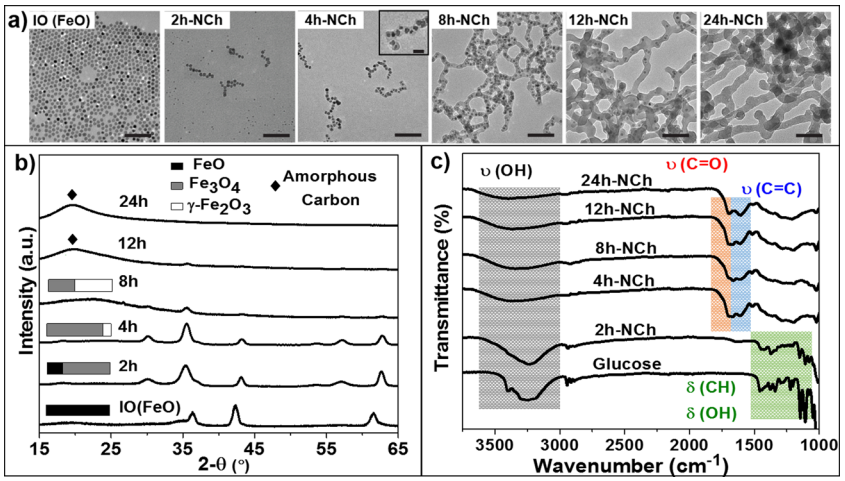

Figure 2. (a) TEM images of the IO (FeO) nanoparticles with an average diameter of 15 nm prior to HTC, and the nanochains succeedingly formed after 2 h, 4 h, 8 h, 12 h, and 24 h of reaction time; the scale bars are 100 nm. (Inset: enlarged TEM image of the 4h-NCh sample showing a visible carbon shell. Scale bar is 20 nm). (b) Powder X-ray diffraction patterns of the nanochains formed at different reaction times. The inset bars represent the iron oxide phase compositions of the nanochains as estimated from Rietveld analysis; the weight percentages for the FeO, Fe_3O_4; and γ-Fe_2O_3 crystalline iron oxide phases are represented in black, gray and white bars, respectively. (c) ATR-FTIR spectra of the nanochains formed at different reaction times.

paramagnetic Fe_3O_4 nanoparticles can act as tiny magnets, which strongly influence the magnetic dipolar interactions among its neighboring IO nanoparticles. As a result, when the Fe_3O_4 nanoparticles were exposed to an organic solvent heated at 140 °C under inert atmosphere conditions, a pronounced clustering of the Fe_3O_4 nanoparticles was observed in comparison to that of the FeO nanoparticles treated under the same conditions (Figure 1a, b). Although the FeO nanoparticles have an innately low saturation magnetization and the interparticle magnetic dipolar interactions might not be sufficiently strong to cause alignment of the particles, FeO can be slowly oxidized into Fe_3O_4 under hydrothermal conditions (Supporting Information Figure S2), which can lead to an increase in saturation magnetization of the overall IO nanoparticle system. This, in turn, can result in a gradual increase in the interparticle magnetic dipolar interactions, which can facilitate a controlled chain-like self-assembly process. As such, by using the nonmagnetic FeO precursor nanoparticles during the HTC of glucose, the fabricated IO@C nanochains are dramatically shorter in length compared to the large IO@C nanochain networks fabricated from the more strongly magnetic Fe_3O_4 nanoparticles (Figure 1a, b). This observation was further confirmed from DLS measurements, whereby a nearly 4-fold increase in nanochain size was observed with the use of the Fe_3O_4 nanoparticles (Figure 1c). Consequently, the IO@C nanochains fabricated using FeO nanoparticles were stable in aqueous suspensions and have unique antibacterial activities compared to the nanochains formed using the Fe_3O_4 nanoparticles.

Because of the better control in magnetic dipolar interactions afforded by the gradual oxidation of the FeO nanoparticles during HTC conditions, the FeO nanoparticles were succeedingly used in the fabrication of a series of carbon nanochains. At the beginning stage, the IO(FeO) precursor nanoparticles were freely dispersed in solution (Figure 2a). The nanoparticles and glucose mixture were then treated hydrothermally for 2 to 24 h at 180 °C. Under hydrothermal conditions, the FeO precursor nanoparticles were slowly transformed into the Fe_3O_4 phase (Figure 2b), while the glucose molecules underwent dehydration, polymerization, intermolecular condensation, and carbonization to form a layer of carbon that encapsulated the IO nanoparticle chain-like assemblies.[23,42,43] After 2 h of reaction time, Rietveld analysis conducted on the powder X-ray diffraction patterns of the samples indicated a phase transformation from 100% FeO to 70% Fe_3O_4 (Figure 2b and Supporting Information Table S1). This conversion of FeO to the Fe_3O_4 crystal structure may be responsible for the enhanced interparticle magnetic dipolar interactions among the IO nanoparticles that induced the formation of short chain-like nanostructures after 2 h of reaction time, resulting in the appearance of IO@C nanochains with an average length of 0.15 μm as evaluated from TEM analysis (Figure 2a). On the other hand, the obtained ATR-FTIR spectrum of the 2h-NCh sample closely resembles the vibrational spectrum of the glucose monomers, with the OH vibrational stretch peak at 3250 cm^{-1} and the δ(CH)/δ(OH) deformation bands in the 1191−1526 cm^{-1} spectral range, indicating that the glucose monomers have not fully polymerized at this stage (Figure 2c). Moreover, some dispersed IO nanoparticles that have not assembled into a chain-like structure were observable in the TEM micrograph (Figure 2a). After 4 h of reaction time, the carbon shell became visible under the TEM (inset, Figure 2a) and the ATR-FTIR spectrum of the 4h-NCh sample revealed a significant loss in the OH vibrational stretch intensity owing to the continued dehydration of the glucose monomers. Moreover, the δ(CH) and δ(OH) deformation bands were replaced with υ(C═O) and υ(C═C) stretch vibration bands (1670 and 1612 cm^{-1}), which supports the emergence of a carbon shell (Figure 2c). As the reaction time increases, the IO nanoparticles continue to oxidize into Fe_3O_4 and γ-Fe_2O_3 (Figure 2b and Supporting Information Table S1). At the same time the carbon coating continues to grow, thereby forming larger and thicker interconnected networks (Figure 2a). After 4 h of HTC, the IO cores were transformed into 92% Fe_3O_4, making the 4h-NCh sample strongly magnetic with a measured saturation magnetization of 95.4 emu/g, a value that is slightly higher compared to noninteracting Fe_3O_4 nanoparticles; this slight

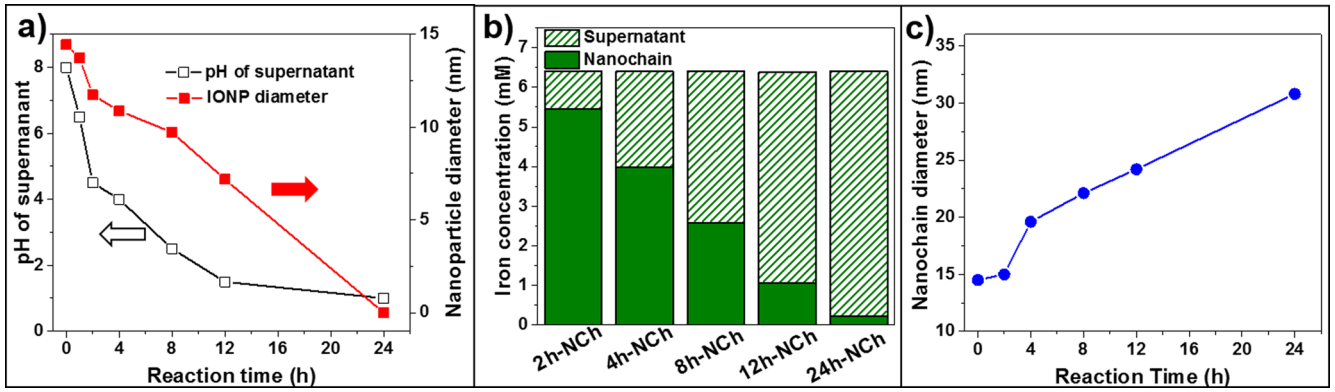

Figure 3. Graphical plots of the reaction progression illustrating (a) the changes in IO core diameters with decreasing pH values of the reaction mixture, respectively, and (b) bar graphs of the Fe elemental analysis results obtained from the isolated nanochains and supernatants at various reaction time points. (c) The changes in nanochain diameter as a function of reaction time.

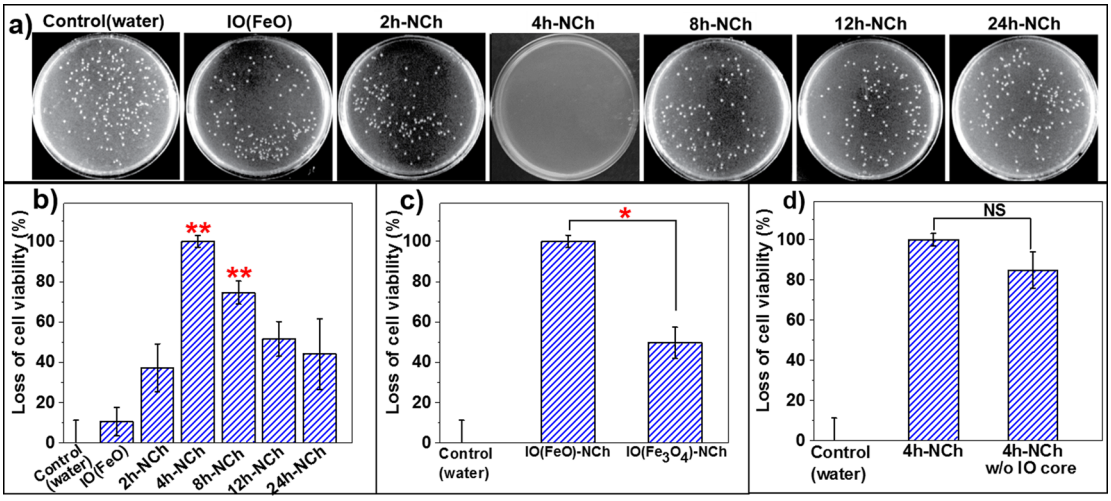

Figure 4. Antibacterial behavior of the synthesized IO@C nanochains against *E. coli.* (a) Photographs showing *E. coli* colonies grown on agar plates after incubation with the different nanochain samples. (b) Loss of cell viability after 15 min incubation time of 8×10^6 *E. coli* bacterial cells with the different carbon nanochain samples (100 μg/mL concentrations). (c) Loss of cell viability after incubation of *E. coli* bacterial cells with nanochains formed from different iron oxide precursors: IO(FeO)-NCh and IO(Fe_3O_4)-NCh. (d) Loss of cell viability comparing the nanochain sample prepared after 4 h of HTC with (4h-NCh) and without IO cores (4h-NCh w/o IO core), respectively. For the cell viability assays, a single asterisk indicates that the results were determined to be statistically significant from each other and NS represents that the results are not statistically significant with p-value less than 0.05 using Student's *t* test, and double asterisks indicate that the result was determined to be statistically significant from the control water treatment with p-value less than 0.05 using a one way analysis of variance (ANOVA) method.

increase in magnetization may be due to the enhanced interparticle dipolar interactions of the coated IO nanoparticles that are locked in place within the hybrid carbon nanochain structure (Supporting Information Figure S3). From TEM analysis, it is evident that the size of the IO cores decreases with reaction time until all of the IO cores completely disappear after 24 h, thus, leaving a pure carbon-based thick nanocable structure (Figure 2a). The observed size reduction of the IO cores can be correlated to the decrease in pH of the reaction mixture, which can be attributed to the emergence of acid decomposition products from the dehydration of glucose (Figure 3a).[42,43] Analysis of the total atomic Fe concentration confirms the dissolution of the nanoparticle templates during the HTC process (Figure 3b). Although it is evident from TEM analysis that the IO cores have completely dissolved after 24 h of reaction time, even with repeated washings a small amount of Fe (0.2 mM) was still measurable from the AAS analysis of the 24h-NCh sample (Figure 3b). This may be attributed to the porous nature of carbon nanomaterials synthesized from the HTC process, which has been shown to be effective in the adsorption of transition metal ions.[44] Overall, the progressive decrease in IO core size and the concomitant increase in Fe concentration found in the supernatants are in agreement with the disappearance of the sharp IO peaks from the powder X-ray diffraction patterns and the emergence of an amorphous carbon peak at 20° (Figure 2b).

Several groups have shown that metal ions can serve as catalysts for the glucose dehydration process during HTC.[26−28] To test this effect, Fe^{2+} and Fe^{3+} ions were separately added during the hydrothermal treatment of glucose. We observed a similar catalytic effect of the Fe ions on the carbonization of glucose, and carbon nanomaterials were isolated after 4 h of reaction time; in comparison, in the absence of the Fe ions, it took 24 h to recover trace amounts of carbon nanomaterials (Supporting Information Figure S4). These results suggest that the Fe ions that leach out from the IO core dissolution during the carbon nanochain formation can continue to participate in the hydrothermal reaction as a catalyst for carbon formation. In

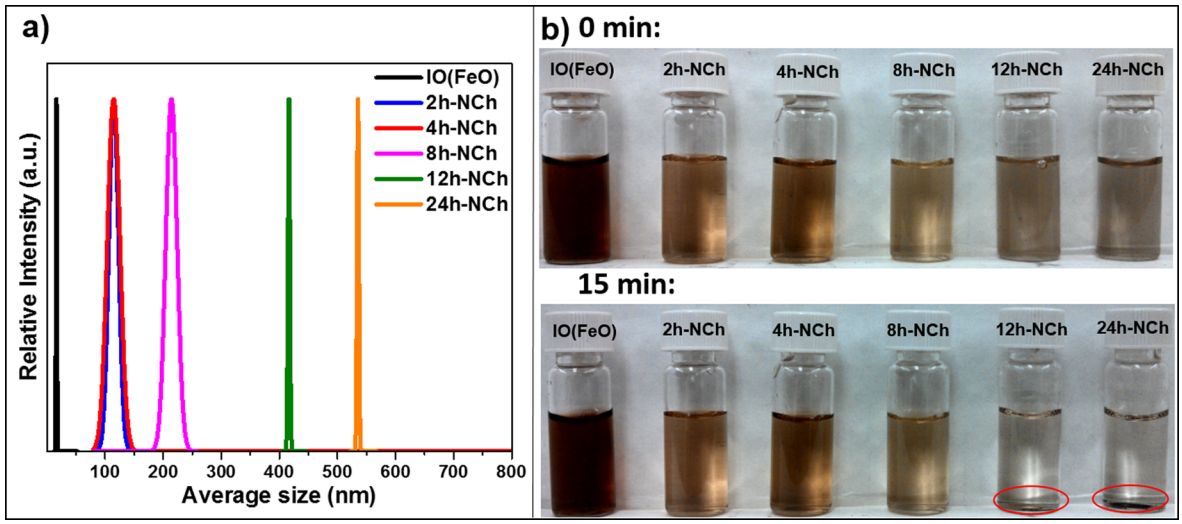

Figure 5. (a) Size distribution of the IO(FeO) nanoparticle and nanochain samples evaluated from DLS measurements. (b) Photographs of the IO(FeO) nanoparticle and nanochain sample solutions after the samples were left to stand at 0 and 15 min, respectively. The red circles indicate nanochain settling in the 12h-NCh and 24h-NCh samples.

turn, as the reaction time proceeds to 8−24 h, the diameter of the nanochains thicken from about 15 to 33 nm, and the initially short-length nanochains formed at 4 h transformed into a large carbon network after 12 to 24 h of reaction times (Figure 3c).

Antibacterial Properties of the IO@C Nanochains. The antibacterial properties of the IO@C nanochains were evaluated using *E. coli* as a test pathogen, a Gram-negative bacterium commonly found in contaminated wastewater. Typical cell viability assays use molecular dyes to measure bacterial cell proliferation,[13] but due to the porous nature of the carbon shell, the dye can be readily adsorbed on the surface of the IO@C nanochains and cause false cell viability measurement results (Supporting Information Figure S5). As such, a colony counting method was adapted in our studies where the bacteria cell viability was estimated through counting of colony forming units (CFUs).[12] The antibacterial effect of the IO@C nanochains prepared at different reaction times was compared to the IO(FeO) precursor nanoparticles with water as control (Figure 4a, b). A series of cell cultures each containing approximately 8×10^6 *E. coli* cells were separately incubated with 100 μg of IO nanoparticle or nanochain sample for 15 min. The bacterial cell incubation studies show a significantly higher loss in cell viability upon exposure with the different IO@C nanochain samples (37.3 to 100.0%) as compared to the bacterial cell death observed upon incubation with the precursor IO(FeO) nanoparticles (10.6%) (Figure 4b). Moreover, the IO@C nanochains fabricated using FeO nanoparticles after 4 h of reaction time [IO(FeO)-NCh] can reach up to a 100.0% loss in cell viability in comparison to only a 49.6% cell death in *E. coli* upon exposure to the nanochain sample synthesized using Fe_3O_4 nanoparticles [IO(Fe_3O_4)-NCh] (Figure 4c). In addition, removal of the IO cores from the 4h-NCh sample did not result in a significant difference in antibacterial activity against *E. coli* (Figure 4d).

The observed increase in antibacterial potency of the hybrid IO@C nanochains compared to the dispersed IO(FeO) nanoparticle sample could be attributed to differences in nanostructure morphology. This observation is in agreement with the studies conducted by Stoehr et al. on the cellular uptake of nanoparticles with various shapes, whereby they demonstrated that wire-like nanoparticles can trigger higher cellular uptake and toxic effects compared to their spherical nanoparticle counterparts.[16] Similarly, although the 2h-NCh and 4h-NCh samples appeared to be similar in size and morphology at first glance, a close examination of the TEM micrograph of the 2h-NCh sample revealed the presence of dispersed nanoparticles that were not enclosed in a carbon nanochain (Figure 2a and Supporting Information Figure S6). This can be due to an incomplete carbonization of glucose after 2 h of reaction time, which is further verified from the comparison of the respective ATR-FTIR spectra of the samples that indicate that the glucose monomers were only completely carbonized after 4 h of reaction time (Figure 2c). As such, we only saw a full carbon shell encapsulation for the nanochains after 4 h of reaction time (inset, Figure 2a).

Previous studies have also highlighted the strong influence of the size of the carbon-based nanomaterial on its antibacterial properties.[11−14] The smaller the size of the carbon nanomaterial, the better is its dispersity and stability in solution, and the larger is the available specific surface area that enables the nanomaterial to better interact with bacterial cells.[11−13] We observed this same effect in our study where the highest loss in cell viability was observed upon treatment with the shortest nanochain sample synthesized using the FeO precursor nanoparticles after 4 h of reaction time. In contrast, treatment with equivalent amounts of nanochains prepared at longer reaction times (12h-NCh and 24h-NCh) resulted in a significantly lower loss in cell viability of 51.6 and 44.1%, respectively (Figure 4b). However, when the concentration of the nanochain sample was increased 10-fold, the larger 24h-NCh nanochain network was also demonstrated to effectively reach 100.0% bacterial cell elimination efficacy (Supporting Information Figure S7). DLS measurements conducted on the different nanochain samples revealed that the chain size increases significantly with prolonged reaction time (Figure 5a). As such, the lower loss in bacterial cell viability could be attributed to the significantly larger chain networks of the samples prepared after 12 and 24 h reaction times. The larger nanochain sizes led to poor water dispersity that is evident from the observation of aggregates that settled down after the samples were left to stand for 15 min at room temperature

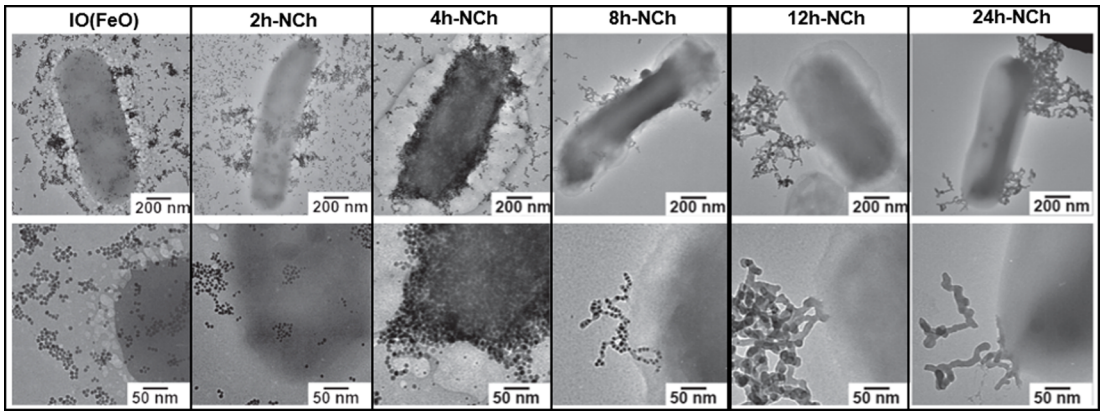

Figure 6. TEM images illustrating the interactions of the synthesized IO(FeO) nanoparticles and carbon nanochains with the cell membrane of *E. coli*. The bottom panels are the corresponding TEM images of the sample interaction with the bacterial cells taken at higher magnification.

(Figure 5b). In contrast, the other nanochain samples prepared at shorter reaction times remained visibly dispersed in solution after 15 min (Figure 5b). By combining the advantages of having a carbonized shell and a short chain-like structure to promote bacterial cell interaction, the 4h-NCh sample can induce the highest *E. coli* cell inactivation percentage among all of the nanochains investigated.

Cytotoxic Mechanism. TEM analysis of the *E. coli* cells exposed to the IO nanoparticles and nanochains reveal that the shortest 4h-NCh sample appears to have the strongest affinity toward the bacterial cell surface (Figure 6). Moreover, in contrast to the other sample treatments whereby the *E. coli* cell membrane remained relatively intact, treatment with the 4h-NCh sample resulted in a visibly disrupted bacterial cell membrane (Figure 6). This result indicates that direct physical membrane disruption of the *E. coli* cells by the nanochains is an important cytotoxic mechanism for effective bacterial cell inactivation. On the other hand, metal oxides have also been demonstrated to be effective agents in killing bacterial cells through the generation of ROS that can induce oxidative stress within the pathogenic cells.[2,45] Moreover, the presence of iron ions can promote Fenton reactions that can lead to enhanced ROS generation.[45,46] In order to investigate the possible contribution of ROS generation by the IO core nanoparticles to the cell inactivation properties of the hybrid IO@C nanochain samples, we have removed the IO cores from the most potent 4h-NCh sample (4h-NCh w/o IO core) prior to bacterial cell incubation.

Despite the absence of the IO cores, a 84.9% loss in cell viability was reached upon treatment with the 4h-NCh without IO core sample. This result was evaluated to be statistically not significant when compared to the loss in cell viability evaluated for the 4h-NCh core−shell sample, thereby implying that under the conditions of our bacterial cell assays, similar antibacterial efficacies can be achieved by the nanochains without the significant influence from the IO cores (Figure 4d). To further examine the possibility of ROS-induced oxidative stress on the *E. coli* cells treated with the different IO nanoparticle and nanochain samples, we performed an XTT assay. XTT is a pale yellow dye that is reduced to a bright orange-colored water-soluble formazan upon reaction with ROS, such as the superoxide anion radical ($O_2^{\bullet-}$). By monitoring the absorption of the generated XTT-formazan at 470 nm, we can monitor the accumulation of ROS. For our study, we used hydrogen peroxide (H_2O_2) as a positive control due to its known capability to induce oxidative stress in various bacterial cell lines.[47−49] We evaluated the ROS generation with varying concentrations of H_2O_2 (0.5, 1.0, and 2.0 mM) using the XTT assay and observed similar results with the different amounts tested (Supporting Information Figure S8). Subsequently, we used the lowest H_2O_2 concentration (0.5 mM) as the positive control in our succeeding XTT assays. After 15 min incubation of the IO nanoparticle and nanochain samples with the XTT dye in the absence of *E. coli* cells, we did not measure any significant absorption signal at 470 nm, which indicates the absence of ROS accumulation (Figure 7). No additional strong

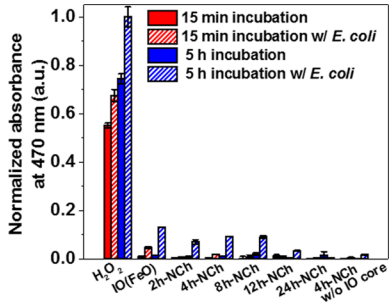

Figure 7. Results of the XTT assay that evaluates the possible generation of ROS in the presence of 100 μg of IO nanoparticle and nanochain samples with and without *E. coli* cells (8×10^6 cells) after 15 min and 5 h incubation time, respectively. All of the measurements were performed in four replicates and determined to be statistically significant from the positive control (H_2O_2, 0.5 mM) with p-value less than 0.05 using a one way analysis of variance (ANOVA) method.

absorption was observed even after a longer incubation time (5 h) in the solutions containing the samples in the absence of the *E. coli* cells (Figure 7). On the other hand, the presence of *E. coli* cells resulted in a minimal increase in absorption signal for the IO(FeO) nanoparticle treated sample, but the changes was marginal indicating that no considerable amount of ROS was generated after 15 min of incubation time. Conversely, after 5 h of incubation of the XTT dye with the IO nanoparticle/nanochain samples in the presence of *E. coli* cells, stronger absorption were monitored at 470 nm, which implies the increased production of ROS at longer incubation time (Figure 7). This was particularly evident in the samples containing large amounts of IO nanoparticle cores [i.e., IO(FeO), 2h-NCh, 4h-NCh, 8h-NCh]. However, the overall absorption signals from the IO nanoparticle/nanochain treated samples were still

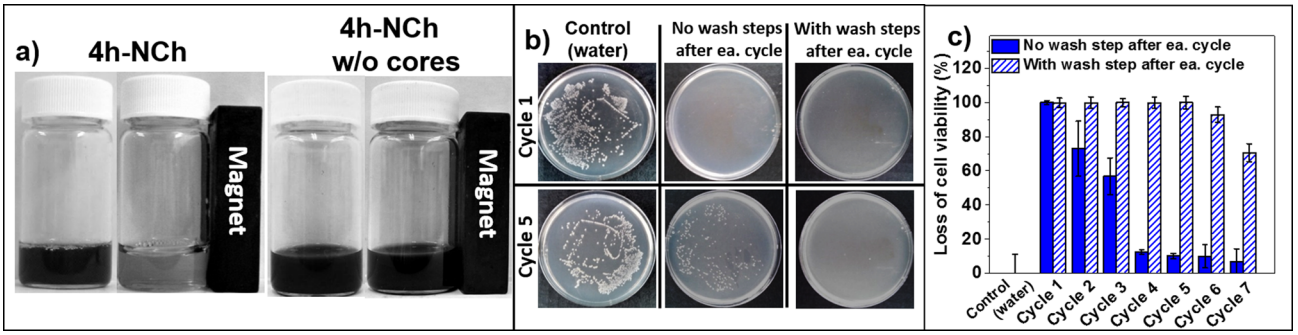

Figure 8. (a) Sample photographs illustrating the magnetic response of the 4h-NCh samples, with and without IO cores, to an external FeNdB bar magnet. (b) Photographs of the cell growth agar plates comparing the antibacterial efficacy of the 4h-NCh samples with and without wash steps in between the different treatment cycles. (c) Comparison of the loss of cell viability between the 4h-NCh samples with and without washing between treatment cycles after seven times exposure to fresh colonies of *E. coli* bacterial cells.

significantly lower compared to the positive control (Figure 7). This result is in agreement with the antibacterial mechanism previously reported by Liu et al. for graphene-based nanomaterials where they did not observed oxidative stress mediated by ROS formation from the carbon-based nanomaterials.[12] In our current study, it appears that at short incubation times (~15 min) ROS generation is minimal and the major cytotoxic mechanism involves the direct physical damage of the bacterial cell membrane upon exposure to the nanochain samples. At longer incubation times (5 h), ROS generation becomes significant for the nanoparticle and nanochain samples with higher IO content, which could lead to oxidative stress in the treated bacterial cells.

IO@C Nanochains As Recyclable Antibacterial Agents. The added benefit with the incorporation of the IO cores is the ability for magnetic separation, which in turn facilitates the recyclability of the fabricated IO@C nanochain antibacterial agents (Figure 8a). After the initial bacterial treatment, the recovered 4h-NCh sample became slightly aggregated and its cell inactivation was significantly reduced (from 100.0 to 72.9%), which may be attributed to adsorbed bacteria cell debris from the previous bacterial treatment (Figure 8b, c and Supporting Information Figure S9). Such effect can be reversed through a washing step with absolute ethanol and water. By performing a wash step between each cycle, the efficiency of the IO@C nanochain sample can be extended and the bacteria-killing performance effectively retained even after five separate treatment cycles (Figures 8b, c). After five cycles, the loss of cell viability showed a slow decline due to a possible loss in the recovered nanochain amount during each washing step.

CONCLUSIONS

In summary, we have developed a new approach toward the fabrication of highly efficient and recyclable IO@C nanochains using a modified hydrothermal carbonization approach. We demonstrated that by using the nonmagnetic FeO precursor nanoparticles during the HTC of glucose monomers, we can have better control of the interparticle magnetic dipolar interactions in the system, thereby enabling the formation of short-length hybrid IO@C nanochains that exhibit potent antibacterial effects. From the performed antibacterial studies against the *E. coli* pathogen, it becomes apparent that the physical disruption of the bacterial cell membrane dominates the cytotoxic effects of the fabricated nanochains. Moreover, we could show that at short incubation times (15 min or less), the core iron oxide nanoparticles do not contribute to a considerable production of ROS that can lead to additional oxidative stress on the bacterial cells. However, the presence of the magnetic iron oxide cores facilitate the magnetic removal and continued reuse of the promising IO@C nanochain antibacterial agents.

ASSOCIATED CONTENT

Supporting Information

Additional data including magnetic hysteresis plots for the FeO and Fe_3O_4 nanoparticles and the IO@C nanochain samples; powder XRD patterns comparing the iron oxide phase composition of the nanoparticle and IO@C nanochain samples exposed to hydrothermal treatment; TEM images and IR spectra of the carbon nanomaterials produced in the presence and absence of Fe ion catalysts; additional TEM images of the nanochain sample; concentration dependent cell studies and result of the fluorescence-based cell assay; XTT assay with different H_2O_2 concentrations. This material is available free of charge via the Internet at http://pubs.acs.org.

AUTHOR INFORMATION

Corresponding Author

*E-mail: anna.samia@case.edu.

Notes

The authors declare no competing financial interest.

ACKNOWLEDGMENTS

This work was supported by a NSF-CAREER Grant (DMR-1253358) from the Solid State and Materials Chemistry Program.

REFERENCES

(1) Mauter, M. S.; Elimelech, M. Environmental Applications of Carbon-Based Nanomaterials. *Environ. Sci. Technol.* **2008**, *42*, 5843−5859.

(2) Wang, Y.-W.; Cao, A.; Jiang, Y.; Zhang, X.; Liu, J.-H.; Liu, Y.; Wang, H. Superior Antibacterial Activity of Zinc Oxide/Graphene Oxide Composites Originating from High Zinc Concentration Localized around Bacteria. *ACS Appl. Mater. Interfaces* **2014**, *6*, 2791−2798.

(3) Tang, J.; Chen, Q.; Xu, L.; Zhang, S.; Feng, L.; Cheng, L.; Xu, H.; Liu, Z.; Peng, R. Graphene Oxide-Silver Nanocomposite as a Highly Effective Antibacterial Agent with Species-Specific Mechanisms. *ACS Appl. Mater. Interfaces* **2013**, *5*, 3867−3874.

(4) Gao, N.; Chen, Y.; Jiang, J. Ag@Fe_2O_3-GO Nanocomposites Prepared by a Phase Transfer Method with Long-Term Antibacterial Property. *ACS Appl. Mater. Interfaces* **2013**, *5*, 11307−11314.

(5) Tian, T.; Shi, X.; Cheng, L.; Luo, Y.; Dong, Z.; Gong, H.; Xu, L.; Zhong, Z.; Peng, R.; Liu, Z. Graphene-Based Nanocomposite as an Effective, Multifunctional, and Recyclable Antibacterial Agent. *ACS Appl. Mater. Interfaces* **2014**, *6*, 8542−8548.
(6) Magrez, A.; Kasas, S.; Salicio, V.; Pasquier, N.; Seo, J. W.; Celio, M.; Catsicas, S.; Schwaller, B.; Forró, L. Cellular Toxicity of Carbon-Based Nanomaterials. *Nano Lett.* **2006**, *6*, 1121−1125.
(7) Li, Q.; Mahendra, S.; Lyon, D. Y.; Brunet, L.; Liga, M. V.; Li, D.; Alvarez, P. J. J. Antimicrobial Nanomaterials for Water Disinfection and Microbial Control: Potential Applications and Implications. *Water Res.* **2008**, *42*, 4591−4602.
(8) Lyon, D. Y.; Alvarez, P. J. J. Fullerene Water Suspension (nC_{60}) Exerts Antibacterial Effects via ROS-Independent Protein Oxidation. *Environ. Sci. Technol.* **2008**, *42*, 8127−8132.
(9) Tu, Y.; Lv, M.; Xiu, P.; Huynh, T.; Zhang, M.; Castelli, M.; Liu, Z.; Huang, Q.; Fan, C.; Fang, H.; Zhou, R. Destructive Extraction of Phospholipids from *Escherichia coli* Membranes by Graphene Nanosheets. *Nat. Nanotechnol.* **2013**, *8*, 594−601.
(10) Mendes, R. G.; Koch, B.; Bachmatiuk, A.; El-Gendy, A. A.; Krupskaya, Y.; Springer, A.; Klingeler, R.; Schmidt, O.; Büchner, B.; Sanchez, S.; Rümmeli, M. H. Synthesis and Toxicity Characterization of Carbon Coated Iron Oxide Nanoparticles with Highly Defined Size Distributions. *Biochim. Biophys. Acta* **2014**, *1840*, 160−169.
(11) Chen, H.; Wang, B.; Gao, D.; Guan, M.; Zheng, L.; Ouyang, H.; Chai, Z.; Zhao, Y.; Feng, W. Broad-Spectrum Antibacterial Activity of Carbon Nanotubes to Human Gut Bacteria. *Small* **2013**, *9*, 2735−2746.
(12) Liu, S.; Zeng, T. H.; Hofmann, M.; Burcombe, E.; Wei, J.; Jiang, R. Antibacterial Activity of Graphite, Graphite Oxide, Graphene Oxide, and Reduced Graphene Oxide: Membrane and Oxidative Stress. *ACS Nano* **2011**, 6971−6980.
(13) Kang, S.; Herzberg, M.; Rodrigues, D. F.; Elimelech, M. Antibacterial Effects of Carbon Nanotubes: Size Does Matter! *Langmuir* **2008**, *24*, 6409−6413.
(14) Kang, S.; Mauter, M. S.; Elimelech, M. Physicochemical Determinants of Multiwalled Carbon Nanotube Bacterial Cytotoxicity. *Environ. Sci. Technol.* **2008**, *42*, 7528−7534.
(15) Ortega, G.; Castaño, D.; Diercks, T.; Millet, O. Carbohydrate Affinity for the Glucose−Galactose Binding Protein is Regulated by Allosteric Domain Motions. *J. Am. Chem. Soc.* **2012**, *134*, 19869−19876.
(16) Stoehr, L. C.; Gonzalez, E.; Stampfl, A.; Casals, E.; Duschl, A.; Puntes, V.; Oostingh, G. J. Shape Matters: Effects of Silver Nanospheres and Wires on Human Alveolar Epithelial Cells. *Part. Fibre Toxicol.* **2011**, *8*, 36.
(17) Adams, C. P.; Walker, K. A.; Obare, S. O.; Docherty, K. M. Size-Dependent Antimicrobial Effects of Novel Palladium Nanoparticles. *PLoS One* **2014**, *9*, e85981.
(18) Zhang, M.; Xie, X.; Tang, M.; Criddle, C. S.; Cui, Y.; Wang, S. X. Magnetically Ultraresponsive Nanoscavengers for Next-Generation Water Purification Systems. *Nat. Commun.* **2013**, *4*, 1866.
(19) Zhang, Z.; Duan, H.; Li, S.; Lin, Y. Assembly of Magnetic Nanospheres into One-Dimensional Nanostructured Carbon Hybrid Materials. *Langmuir* **2010**, *26*, 6676−6680.
(20) Zhu, J.; Wei, S.; Gu, H.; Rapole, S. B.; Wang, Q.; Luo, Z.; Haldolaarachchige, N.; Young, D. P.; Guo, Z. One-Pot Synthesis of Magnetic Graphene Nanocomposites Decorated with Core@Double-Shell Nanoparticles for Fast Chromium Removal. *Environ. Sci. Technol.* **2012**, *46*, 977−985.
(21) Zhang, W.-H.; Liang, C.; Sun, H.; Shen, Z.; Guan, Y.; Ying, P.; Li, C. Synthesis of Ordered Mesoporous Carbons Composed of Nanotubes via Catalytic Chemical Vapor Deposition. *Adv. Mater.* **2002**, *14*, 1776−1778.
(22) Liu, Z.; Zhou, X.; Qian, Y. Synthetic Methodologies for Carbon Nanomaterials. *Adv. Mater.* **2010**, *22*, 1963−1966.
(23) Titirici, M.-M.; Antonietti, M. Chemistry and Materials Options of Sustainable Carbon Materials Made by Hydrothermal Carbonization. *Chem. Soc. Rev.* **2010**, *39*, 103−116.
(24) Jafari, A.; Boustani, K.; Farjami Shayesteh, S. Effect of Carbon Shell on the Structural and Magnetic Properties of Fe_3O_4 Superparamagnetic Nanoparticles. *J. Supercond. Novel Magn.* **2013**, *27*, 187−194.
(25) Zhang, W.; Jia, S.; Wu, S.; Zhang, S.; Liu, Y. Effects of Alkaline Precipitating Agents on Synthesis of Magnetite Nanomaterials by Hydrothermal D-Glucose Method. *J. Nanopart. Res.* **2013**, *15*, 1701.
(26) Zheng, C.; Chen, P.; Bao, S.; Xia, J.; Sun, X. Environmentally Compatible Synthesis of Superparamagnetic Magnetite (Fe_3O_4) Nanoparticles with Prehydrolysate from Corn Stover. *BioResources* **2013**, *9*, 589−601.
(27) Cui, X.; Antonietti, M.; Yu, S.-H. Structural Effects of Iron Oxide Nanoparticles and Iron Ions on the Hydrothermal Carbonization of Starch and Rice Carbohydrates. *Small* **2006**, *2*, 756−759.
(28) Gao, J.; Zhang, B.; Zhang, X.; Xu, B. Magnetic-Dipolar-Interaction-Induced Self-Assembly Affords Wires of Hollow Nanocrystals of Cobalt Selenide. *Angew. Chem., Int. Ed. Engl.* **2006**, *45*, 1220−1223.
(29) Klokkenburg, M.; Vonk, C.; Claesson, E. M.; Meeldijk, J. D.; Erné, B. H.; Philipse, A. P. Direct Imaging of Zero-Field Dipolar Structures in Colloidal Dispersions of Synthetic Magnetite. *J. Am. Chem. Soc.* **2004**, *126*, 16706−16707.
(30) Varón, M.; Beleggia, M.; Kasama, T.; Harrison, R. J.; Dunin-Borkowski, R. E.; Puntes, V. F.; Frandsen, C. Dipolar Magnetism in Ordered and Disordered Low-Dimensional Nanoparticle Assemblies. *Sci. Rep.* **2013**, *3*.
(31) Jonsson, T.; Nordblad, P.; Svedlindh, P. Dynamic Study of Dipole−Dipole Interaction Effects in a Magnetic Nanoparticle System. *Phys. Rev. B* **1998**, *57*, 497−504.
(32) Mørup, S.; Hansen, M. F.; Frandsen, C. Magnetic Interactions between Nanoparticles. *Beilstein J. Nanotechnol.* **2010**, *1*, 182−190.
(33) Hill, L. J.; Pyun, J. Colloidal Polymers via Dipolar Assembly of Magnetic Nanoparticle Monomers. *ACS Appl. Mater. Interfaces* **2014**, *6*, 6022−6032.
(34) Pablico-Lansigan, M. H.; Situ, S. F.; Samia, A. C. S. Magnetic Particle Imaging: Advancements and Perspectives for Real-Time In Vivo Monitoring and Image-Guided Therapy. *Nanoscale* **2013**, *5*, 4040−4055.
(35) Park, J.; An, K.; Hwang, Y.; Park, J.-G.; Noh, H.-J.; Kim, J.-Y.; Park, J.-H.; Hwang, N.-M.; Hyeon, T. Ultra-Large-Scale Syntheses of Monodisperse Nanocrystals. *Nat. Mater.* **2004**, *3*, 891−895.
(36) Feng, Z.; Zhu, S.; Martins de Godoi, D. R.; Samia, A. C. S.; Scherson, D. Adsorption of Cd^{2+} on Carboxyl-Terminated Superparamagnetic Iron Oxide Nanoparticles. *Anal. Chem.* **2012**, *84*, 3764−3770.
(37) Kim, W.; Suh, C.-Y.; Cho, S.-W.; Roh, K.-M.; Kwon, H.; Song, K.; Shon, I.-J. A New Method for the Identification and Quantification of Magnetite−Maghemite Mixture Using Conventional X-ray Diffraction Technique. *Talanta* **2012**, *94*, 348−352.
(38) Fisichella, M.; Berenguer, F.; Steinmetz, G.; Auffan, M.; Rose, J.; Prat, O. Toxicity Evaluation of Manufactured CeO_2 Nanoparticles Before and After Alteration: Combined Physicochemical and Whole-Genome Expression Analysis in Caco-2 Cells. *BMC Genomics* **2014**, *15*, 700.
(39) Dumas, E.-M.; Ozenne, V.; Mielke, R. E.; Nadeau, J. L. Toxicity of CdTe Quantum Dots in Bacterial Strains. *IEEE Trans. Nanobiosci.* **2009**, *8*, 58−64.
(40) Lyon, D. Y.; Brunet, L.; Hinkal, G. W.; Wiesner, M. R.; Alvarez, P. J. J. Antibacterial Activity of Fullerene Water Suspensions (nC_{60}) Is Not Due to ROS-Mediated Damage. *Nano Lett.* **2008**, *8*, 1539−1543.
(41) Hou, Y.; Xu, Z.; Sun, S. Controlled Synthesis and Chemical Conversions of FeO Nanoparticles. *Angew. Chem., Int. Ed. Engl.* **2007**, *46*, 6329−6332.
(42) Sevilla, M.; Fuertes, A. B. The Production of Carbon Materials by Hydrothermal Carbonization of Cellulose. *Carbon* **2009**, *47*, 2281−2289.
(43) Baccile, N.; Laurent, G.; Babonneau, F.; Fayon, F.; Titirici, M.-M.; Antonietti, M. Structural Characterization of Hydrothermal

Carbon Spheres by Advanced Solid-State MAS ^{13}C NMR Investigations. *J. Phys. Chem. C* **2009**, *113*, 9644−9654.
(44) Nata, I. F.; Salim, G. W.; Lee, C.-K. Facile Preparation of Magnetic Carbonaceous Nanoparticles for Pb^{2+} Ions Removal. *J. Hazard. Mater.* **2010**, *183*, 853−858.
(45) Keenan, C. R.; Sedlak, D. L. Factors Affecting the Yield of Oxidants from the Reaction of Nanoparticulate Zero-Valent Iron and Oxygen. *Environ. Sci. Technol.* **2008**, *42*, 1262−1267.
(46) Tran, N.; Mir, A.; Mallik, D.; Sinha, A.; Nayar, S.; Webster, T. J. Bactericidal Effect of Iron Oxide Nanoparticles on *Staphylococcus Aureus*. *Int. J. Nanomedicine* **2010**, *5*, 277−283.
(47) Zhou, A.; He, Z.; Redding-Johanson, A. M.; Mukhopadhyay, A.; Hemme, C. L.; Joachimiak, M. P.; Luo, F.; Deng, Y.; Bender, K. S.; He, Q.; Keasling, J. D.; Stahl, D. A.; Fields, M. W.; Hazen, T. C.; Arkin, A. P.; Wall, J. D.; Zhou. Hydrogen Peroxide-Induced Oxidative Stress Responses in *Desulfovibrio vulgaris Hildenborough*. *J. Environ. Microbiol.* **2010**, *12*, 2645−2657.
(48) González-Párraga, P.; Hernández, J. A.; Argüelles, J. C. Role of Antioxidant Enzymatic Defences Against Oxidative Stress H_2O_2 and the Acquisition of Oxidative Tolerance in *Candida Albicans*. *Yeast* **2003**, *20*, 1161−1169.
(49) Davies, K. J. The Broad Spectrum of Responses to Oxidants in Proliferating Cells: A New Paradigm for Oxidative Stress. *IUBMB Life* **1999**, *48*, 41−47.